Title

Functional-structural root system model validation using soil MRI and tracer experiment

Downloaded from https://academic.oup.com/jxb/advance-article-abstract/doi/10.1093/jxb/erz060/5336523 by The University of British Columbia Library user on 19 February 2019

Authors and affiliations

Axelle Koch[1], Félicien Meunier[1,2], Jan Vanderborght[3,4], Sarah Garré[5], Andreas Pohlmeier[3] and Mathieu Javaux[1,3*]

[1] Earth and Life Institute- Environmental sciences, UCLouvain, Croix du Sud 2 L7.05.02, BE-1348 Louvain-la-Neuve, Belgium

[2] Computational and Applied Vegetation Ecology lab, Ghent University, Coupure Links 653, BE-9000 Ghent, Belgium

[3] Institute of Bio- and Geosciences, IBG-3 Agrosphere, Forschungszentrum Jülich GmbH, D-52425 Jülich, Germany

[4] Earth and Environmental Sciences, KULeuven, Celestijnenlaan 200/2411, BE-3001 Leuven, Belgium

[5] Gembloux Agro-Bio Tech, Université de Liège, Passage des déportés 2, BE-5030 Gembloux, Belgium

[*] Corresponding author: +32 10 47 37 08

axelle.koch@uclouvain.be

felicien.meunier@ugent.be

j.vanderborght@fz-juelich.de

sarah.garre@uliege.be

a.pohlmeier@fz-juelich.de

mathieu.javaux@uclouvain.be

Accepted Manuscript

Journal

Journal of Experimental Botany

© The Author(s) 2019. Published by Oxford University Press on behalf of the Society for Experimental Biology.

This is an Open Access article distributed under the terms of the Creative Commons Attribution License (http://creativecommons.org/licenses/by/4.0/), which permits unrestricted reuse, distribution, and reproduction in any medium, provided the original work is properly cited.

Submission date: 22/08/2018

1 table, 9 figures (7 in colors)

6442 words

Supplementary data: 1 video, 3 figures, 2 tables

Accepted Manuscript

Downloaded from https://academic.oup.com/jxb/advance-article-abstract/doi/10.1093/jxb/erz060/5336523 by The University of British Columbia Library user on 19 February 2019

Highlight

We validated for the very first time a functional-structural root system model by combining a tracer experiment monitored with magnetic resonance imaging and three-dimensional modeling of water and solute transport.

Abstract

Functional-structural root system models simulate the relations between root system architectural and hydraulic properties, and the spatio-temporal distributions of water and solute in the root zone. Such models might help identify optimal plant properties for breeding and contribute to increased water use

efficiency. However, it must be first demonstrated that they accurately reproduce the processes they intend to describe. This is challenging because the flow and transport processes towards individual roots are hard to observe. We demonstrate how this deadlock could be broken by combining co-registered root and tracer distributions obtained from magnetic resonance imaging with a root system model in an inverse modeling scheme. The main features in the tracer distributions were well reproduced by the model using realistic root hydraulic parameters. By combining functional-structural root system model with 4D tracer observations, we were able to quantify the water uptake distribution of a growing root system. We showed that 76% of the transpiration was extracted through 3rd order roots. The simulations also demonstrated that accurate water uptake distribution cannot be directly derived neither from observations of tracer accumulation nor from water depletion. However, detailed tracer experiments combined with process-based models help decipher mechanisms underlying root water uptake.

Key words

Functional-structural root system model; magnetic resonance imaging; root hydraulic conductivities; root water uptake; R-SMWS; tracer experiment

List of abbreviations

2D/3D/4D = Two/Three/Four-dimensional

DaS = Days after Sowing

FSRSM = Functional-Structural Root System Model

FOV = Field Of View

Gd-DTPA^{2-} = Gadolinium Diethylene-Triamine-Penta-Acetate

MRI = Magnetic Resonance Imaging

Neutron CT = neuton computed tomography

RMSE = Root Mean Square of Error

RSA = Root System Architecture

RWU = Root Water Uptake

SPAC = Soil-Plant-Atmosphere Continuum

X-ray CT = X-ray computed tomography

Accepted Manuscript

Downloaded from https://academic.oup.com/jxb/advance-article-abstract/doi/10.1093/jxb/erz060/5336523 by The University of British Columbia Library user on 19 February 2019

1 Introduction

Functional-structural root system models (FSRSM, see Ndour et al. 2017; Meunier et al. 2017) have been developed since the late 80ies (Diggle 1988; Doussan et al. 2006; Javaux et al. 2008; Schnepf et al. 2018). These models combine root functional and structural information to describe local processes in the soil-root continuum (Passot et al. 2018). They aim to better understand the relationships between root architecture, root development, hydraulics and water flow and solute transport in the root zone.

Resolving processes around roots indeed helps understand, amongst others, (i) the root hydraulic architecture development (Zarebanadkouki et al. 2016), (ii) the impact of salinity stress (Schröder et al. 2013; Jorda et al. 2018), (iii) the fate of pesticides in the root zone, (iv) the nutrient uptake (Dunbabin et al. 2004; Leitner et al. 2010), (v) the strategies developed by plants competing for resource acquisition (Postma & Lynch 2012; Li et al. 2015; Li et al. 2016; Strock et al. 2018), (vi) the interactions between soil structure and root growth (Landl et al. 2016), or (vii) the impact of mucilage in root water uptake (Schwartz et al. 2016). Moreover, these models can be used for optimizing root traits and develop crop ideotypes (Leitner et al. 2014; Meunier et al. 2016).

However, the accuracy of FSRSM to predict root water uptake (RWU) of a complex root system has never been validated with four-dimensional (4D, time and space) experimental data so far. Indeed, Schröder et al. (2013) proved the ability of R-SWMS (Javaux et al. 2008) to predict steady state salt accumulation around a single root but not around an actual growing root system. Koebernick et al. (2015) simulated water uptake with a FSRSM, using 4D root system architecture (RSA) that were derived from computed tomography measurements. Yet, the measured soil variables (i.e. the soil water potential) that were compared with simulation results were not spatially resolved around single roots but represented bulk soil measurements. Zarebanadkouki et al. (2016) did obtain spatially resolved information about the RSA and the water flow into roots from imaging the movement of deuterated water with neutron radiography. However, these techniques are limited to 3D experiments (2D space and time).

Experimental data on RWU and root hydraulic properties are required for a direct validation, which is very challenging to obtain. On one hand, measuring the magnitude and the spatial distribution of RWU remains complex and tedious despite the technical progress achieved in the past decades to directly observe water movement in the soil-plant-atmosphere continuum (SPAC, Ahmed et al. 2015). On the other hand, while being emphasized as critical for plant performance (Leitner et al. 2014), root hydraulic properties remain difficult to characterize for several reasons (Vadez 2014). First, their determination is highly time-consuming (Li & Liu 2010). Therefore, it is difficult to repeat them over to the entire set of root ages, orders and development stages. Secondly, while it has been demonstrated that these properties change

Accepted Manuscript

Downloaded from https://academic.oup.com/jxb/advance-article-abstract/doi/10.1093/jxb/erz060/5336523 by The University of British Columbia Library user on 19 February 2019

dramatically with root type, root age (Vetterlein & Doussan 2016), and might be affected by environmental constraints (Hachez et al. 2012), current experimental techniques are rather local. As a consequence, there is currently no agreement on a standard methodology to measure the distribution of root hydraulic conductivities in a whole root system (Rieger & Litvin 1999; Meunier et al. 2018a).

This lack of information on RWU distribution and on root hydraulic properties hinders the validation of FSRSMs in a direct way. However, an indirect validation is still within reach by combining simulations and observations in an inverse modeling framework. In inverse modeling, the modeled outputs are compared to the experimental results and the error between them is calculated. This is repeated with varying model parameters until a minimal error or an error lower than a previously defined threshold value is reached. In other words, inverse modeling allows deriving information, from the outputs, on the model input parameters. In case of a process-based model, it is assumed that the key processes are accurately simulated by the model. Inversion leading to a physically- (or physiologically-) based set of parameters therefore indirectly validates the used FSRSM.

An accurate FSRSM validation through inverse modeling, while possible, requires yet an important experimental setup. First, three to four-dimensional (3D space with or without time) RSA is required. Nowadays, various non-invasive techniques allow RSA acquisition, such as Magnetic Resonance Imaging (MRI, Stingaciu et al. 2013), X-ray Computed Tomography (X-ray CT, Mairhofer et al. 2012; Koebernick et al. 2014), neutron Computed Tomography (neutron CT, Moradi et al. 2011) or the combination of RGB and hyperspectral imaging (Bodner et al. 2017). Then information about root zone processes (e.g. water content, water potential or tracer dynamics) is needed. Spatio-temporal distributions of water content can be obtained using X-ray CT (Hainsworth & Aylmore 1983), neutron CT (Carminati et al. 2010; Esser et al. 2010; Tötzke et al. 2017), and MRI (Pohlmeier 2010). But, water content patterns do not contain a lot of information about the actual distribution of the water fluxes and local uptake rates (Vandoorne et al. 2012). Imaging tracer distributions could be an alternative to derive indirectly distributions of water fluxes and could therefore be used to validate FSRSMs. Zarebanadkouki et al. (2012; 2013; 2014) and Tötzke et al. (2017) tracked deuterated water transport through the SPAC with neutron radiography and were able to quantify local RWU. More recently, MRI has been used to track Gd-DTPA^{2-} fate in a sandy soil column (Haber-Pohlmeier et al. 2017), offering the opportunity to determine when and where (i.e. by which roots) water was actually taken up.

In this study, we intend to numerically reproduce tracer movement in a sand container planted with *Lupinus albus* L. as designed by Haber-Pohlmeier et al. (2017). We investigated how the 4D monitoring of that tracer in combination with process-based modeling could inform us about RWU dynamics and plant hydraulic properties. In particular, we focused on the inverse modeling of the tracer distribution and accumulation to retrieve the hydraulic properties of the root system using a physically-based model of the water flow in the

Accepted Manuscript

Downloaded from https://academic.oup.com/jxb/advance-article-abstract/doi/10.1093/jxb/erz060/5336523 by The University of British Columbia Library user on 19 February 2019

SPAC. The objective of this work is therefore threefold. We aim to (i) validate a FSRSM for water flow and solute transport in the root zone, (ii) determine how informative the evolution of a tracer distribution is for the RWU dynamics of a growing root system, and (iii) retrieve the most likely distribution of root hydraulic properties.

Accepted Manuscript

Downloaded from https://academic.oup.com/jxb/advance-article-abstract/doi/10.1093/jxb/erz060/5336523 by The University of British Columbia Library user on 19 February 2019

2 Materials and methods

2.1 Experimental setup

We briefly summarize hereafter the experimental setup. For more detailed information, we refer to Haber-Pohlmeier et al. (2017). A 7-day tracer experiment was performed in a column planted with white lupine (*Lupinus albus* L.) and root development, water content and tracer concentration distributions were monitored over time by MRI.

After seed germination, the white lupine plant was grown for 18 days in a cylindrical column (10 cm high; 5 cm inner diameter, see Figure 1) filled with sand (FH31, Quarzwerke Frechen GmbH, Frechen, Germany) under a 12h/12h day-night lighting cycle at 60% relative humidity. The cylindrical shape of the column and the use of sandy medium are constraints linked to MRI technology. The tracer experiment started afterwards, i.e. 18 days after sowing (DaS, see Figure S1). We used gadolinium diethylene-triamine-penta-acetate ($Gd\text{-}DTPA^{2-}$), which is an MRI contrast agent that can be used as a tracer for solute transport in porous media thanks to its chemical inertness, its conservative transport properties, and its anionic net charge in neutral aqueous solution that prevents its adsorption on soil mineral surfaces (Haber-Pohlmeier et al. 2010). The imaged initial volumetric soil water content (θ see list of variables, Table 1) was 0.35 ($cm^3\ cm^{-3}$). During the first six days of experiment (from 18 to 24 DaS), the soil column was located under artificial lights (PAR sufficient for the plant to transpire and grow) and irrigated continuously with a 1 mmol L^{-1} $Gd\text{-}DTPA^{2-}$ solution, except for the MRI scanning periods (~6 h/day). The plant was not transpiring nor watered during the scanning periods, which were performed overnight. During the last day of experiment (from 24 to 25 DaS), irrigation was stopped so that the tracer and the water could redistribute in the sand substrate. The main driver of water movement in the column was then the plant transpiration. The cumulative fluxes of irrigation solution, transpired water and effluent, together with the mean column water content, are detailed in Table S1, as they were observed or calculated (adapted from Haber-Pohlmeier et al. (2017)). The soil-root system was imaged daily during the entire experiment in order to obtain tracer and root distribution maps. However, due to technical problems with the scanner, no image was obtained the sixth day of the experiment (at 24 DaS). The experiment protocol and timing are summarized in Figure S1.

The scanner used for imaging the RSA and the tracer concentration in the liquid phase was a 1.5 T split-coil MRI scanner (Agilent Technologies) comprising a 300 mT/m gradient system and a 10 cm solenoid transmitter-receiver coil. The RSA was imaged using a T_2 (the transverse relaxation time) weighted 3D fast spin echo imaging sequence with a matrix size of 256 x 256 x 64 points for a field of view (FOV) of 60 x 60 x 70.4 mm^3. The FOV started from the top of the soil column. The maps of $Gd\text{-}DTPA^{2-}$ concentration in the liquid phase were acquired from 2D multislice spin echo sequence with inversion recovery preparation. The axial FOV was 60 x 60 mm^2 with a matrix size of 256 x 256 points, and forty axial slices of thickness 2 mm

Accepted Manuscript

Downloaded from https://academic.oup.com/jxb/advance-article-abstract/doi/10.1093/jxb/erz060/5336523 by The University of British Columbia Library user on 19 February 2019

and 0.2 mm gap were imaged. The resulting spatial resolution of the voxels is 0.234 x 0.234 x 2.2 mm^3. Both matrices (RSA and Gd-$DTPA^{2-}$ concentration) are concentric. This means that the upper slice of the RSA matrix corresponds to the fifth slice of the Gd-$DTPA^{2-}$ concentration maps.

2.2 Reconstruction of RSA

The reconstruction of the RSA was based on the previously described MRI measurements conducted by Haber-Pohlmeier et al. (2017). First, the MRI data were processed and segmented into binary images. We then reconstructed the RSA manually and extracted the root segment network. This was achieved on a Holobench, a 3D virtual reality system that runs on VISTA-Software (VISTAWurzel). We used 3D-polarized glasses and a 3D-computer mouse to track each root branch 3D location and radius from the binary images (Stingaciu et al. 2013; Koebernick et al. 2015). One should notice that MRI could not detect roots that had a diameter smaller than 200 µm.

To characterize the growing RSA, we started the reconstruction with the root system of the last day (MRI image taken at 25 DaS) and continued in inverse chronological order (MRI images taken at 23, 22, 21, 20, 19 and 18 DaS) by removing the last created root nodes step by step. After that, root origination time and branching order were linearly interpolated with MATLAB routines between successive images.

2.3 Models coupling and setup

R-SWMS (Javaux et al. 2008), a model that computes soil water flow based on Richards equation and 3D water flow in the root system based on an explicit consideration of water potential gradients, was used to simulate the experiment. For representing tracer transport, R-SWMS was coupled with ParTrace (Schröder et al. 2012), which solves the convection-dispersion equation based on a Lagrangian approach (random walk particle tracking). R-SWMS provides ParTrace with the water content distribution as well as the velocity field, with which ParTrace simulates the particle movements and calculates the concentration distributions.

Since the mesh in R-SWMS is composed of cubic voxels, representing a cylinder would require an infinite number of voxels. A mesh of cubic 0.25 x 0.25 x 0.25 cm^3 voxels was the chosen compromise between computational power and accurate representation of the cylindrical shape. Given the square shape of the grid elements, the simulated column surface area was slightly different from the one of the experimental column (Figure 1). Therefore, the simulated input, output and transpiration flows were adapted with the following weighting factor:

$$W_{simulation} = \frac{A_{simulation}}{A_{experiment}} * W_{experiment} \quad \text{(Equation 1)}$$

Accepted Manuscript

Downloaded from https://academic.oup.com/jxb/advance-article-abstract/doi/10.1093/jxb/erz060/5336523 by The University of British Columbia Library user on 19 February 2019

with W the water flows (irrigation, effluent or transpiration flows, see Figure 1) and A the soil column surface. For a voxel size of 0.25 cm, the ratio between simulated and experimental surfaces ($\frac{A_{simulation}}{A_{experiment}}$) is 1.1. In addition, in the schematics of Figure 1, we give the axis convention for R-SWMS. The vertical axis (called z) is positive upwards. Therefore, in the following, xy- or horizontally-averaged are used equivalently.

Soil hydraulic properties were modeled using the closed-form equations of van Genuchten-Mualem (Mualem 1976; van Genuchten 1980) and these functions were parameterized according to Schröder (2014) who worked with the same soil (see soil properties, Table S2). Soil bulk density (ρ_b) was set in the model to 1.62 g cm^{-3}, its measured value. Regarding the solute transport parameters, the diffusivity of Gd-$DTPA^{2-}$ was fixed to 0.35 cm^2 day^{-1} as in Bechtold et al. (2011). The longitudinal (α_L) and lateral (α_T) dispersivities were set to 0.25 cm and 0.025 cm, respectively. The longitudinal dispersivity value was set to its maximal theoretical value, the voxel width (0.25 cm). Solute was considered not to be taken up by roots (i.e. exclusion). An analysis of Gd-$DTPA^{2-}$ mass balance at the end of the experiment showed that this assumption was true (Haber-Pohlmeier et al. 2017).

Root growth and aging were explicitly simulated using linear interpolations between successive MRI root system scans as explained in section 2.2.

2.4 Analyses

Determining optimal root hydraulic properties

Two hydraulic parameters were defined for each single root segment: the radial conductivity (k_r) and the axial conductance (K_x). These properties depend on the root order and the segment age (Doussan et al. 2006; Zarebanadkouki et al. 2016). To avoid a too large set of possible root architectures, we constrained their distributions according to several assumptions. First, we assumed that k_r and K_x were constant along the taproot as in Zarebanadkouki et al. (2016). For the laterals (root orders 2 and 3), we assumed that the root segments younger than 5 days-old had different hydraulic parameters than older root segments. The stepwise response of RWU to the root development processes supports that assumption (Vetterlein & Doussan 2016). Furthermore, k_r of the older segments had to be smaller than that of younger ones. Indeed, the formation of the casparian band, which hinders water to follow the apoplastic pathway from the cortex to the stele, increases the root resistance to radial flow (Vetterlein & Doussan 2016). Below, the hydraulic properties of the taproot will be assigned by the subscript T and those of the lateral roots by the subscripts Ly and Lo for the young (0-5 days old) and the old root segments (5-25 days old), respectively. The 5 days-old threshold was chosen to have similar root length for both age classes. The sets of tested radial conductivities and axial conductances were geometric sequences in the intervals [10^{-5} 10^{2}] (cm hPa^{-1} day^{-1})

Accepted Manuscript

Downloaded from https://academic.oup.com/jxb/advance-article-abstract/doi/10.1093/jxb/erz060/5336523 by The University of British Columbia Library user on 19 February 2019

and [10^{-4} 10^{2}] (cm^4 hPa^{-1} day^{-1}), respectively. The resulting simulated Gd-DTPA^{2-} concentration maps, corresponding to the 15750 generated scenarios differing only in their root hydraulics parameterization, were compared to the experimental distribution.

To assess the fitness of a certain root hydraulic architecture to describe the observed tracer concentration distribution, Root Mean Square of the Error (RMSE) between simulated and observed spatial tracer concentration maps, was used and calculated as:

$$RMSE = \sqrt{\frac{\sum_{i=1}^{N}([Gd-DTPA^{2-}]_{obs,i}-[Gd-DTPA^{2-}]_{mod,i})^2}{N}} \quad \text{(Equation 2)}$$

with [Gd-DTPA^{2-}]$_{obs,i}$ and [Gd-DTPA^{2-}]$_{mod,i}$ the observed and modeled concentration in voxel i, respectively, and N the total number of observed voxels. Since the spatial resolution differed between observed and modeled [Gd-DTPA^{2-}] maps, the MRI results were averaged to match the simulated grid.

The simulated Gd-DTPA^{2-} maps were considered at the time corresponding to the end of the MRI scanning. Only the last day of the irrigation treatment and the non-leaching phase were simulated for the parameter optimization. Indeed, water movement (and hence tracer transport) mainly depended on soil characteristics during the leaching period (between 18 and 24 DaS), whereas it depended more on root properties during the non-leaching period (between 24 and 25 DaS), throughout which plant transpiration was the main water movement driver. However, since the Gd-DTPA^{2-} distribution map at 24 DaS was not available (as the MRI facility did not work that particular day), we started the simulation at 23 DaS. Initial (soil water content distribution, solute distribution and root architecture at 23 DaS) and boundary (irrigation, transpiration and effluent flows) conditions were defined according to the experimental conditions. As mentioned earlier, the Gd-DTPA^{2-} concentration maps obtained by MRI did not cover the entire soil column. Therefore, to generate the initial concentration distribution file, we calculated the quantity of Gd-DTPA^{2-} contained in the entire soil volume (difference between the amount of tracer present in the cumulative irrigated solution and in the cumulative effluent), we determined how much Gd-DTPA^{2-} was located in the part of the soil column that was imaged by MRI and we added the difference in the non-monitored soil area. The tracer concentration was assumed to be uniformly distributed within the xy-layer and to linearly decrease with depth (see Figure 2A).

As, in R-SWMS, the roots do not occupy any explicit volume, Gd-DTPA^{2-} could accumulate exactly where the water is taken up (at root nodes) whereas, in reality, the accumulation occurs around the root boundaries. This may introduce an overestimation of the actual Gd-DTPA^{2-} concentration if the model spatial resolution is too fine. Indeed, when considering voxels of 0.25 cm width, root segments occupied in average 1/2, 1/4,

Accepted Manuscript

Downloaded from https://academic.oup.com/jxb/advance-article-abstract/doi/10.1093/jxb/erz060/5336523 by The University of British Columbia Library user on 19 February 2019

or 1/5 of the voxel volume for order 1, 2 and 3 respectively. For that reason, the comparison was computed for merged voxels (0.5 cm width).

The best (i.e. which lead to the lowest RMSE) parameter set was further locally optimized by exploring the parameter space with smaller and smaller ranges around the minimum until convergence.

Experiment sensitivity to root hydraulic properties

To determine the information content of the MRI experiment, a local sensitivity analysis was performed around the global optimum to assess to which root hydraulic parameters the dataset is sensitive. To do so, 1215 parameter sets were generated by systematically sampling 2D parameter cross-sections of the parameter space around the global optimum. The parameter domain was fixed in a range corresponding to 1/8 to 8 times the optimal parameters. The 3D tracer distribution sensitivity to root hydraulic properties was checked using the RMSE between the observed and the simulated values (Equation 2).

Evaluating water uptake proxies

The model was then run over the entire experimental period (i.e. between 18 and 25 DaS) with the optimized parameters and with the same initial and boundary conditions as the experiment. This allowed us to determine the water uptake density (WUD) distribution and dynamics. WUD is the volumetric flow of uptake per soil voxel volume [cm^3_{water} day^{-1} cm^{-3}_{soil}]. Since the tracer is supposed to be inert and not extracted by plant roots, solute should preferentially accumulate where the plant extracts soil water. If that hypothesis is confirmed, then the solute distribution map, obtained by MRI, informs us about cumulative WUD distribution. We also focused on determining what relationships existed between water depletion (WD, i.e. water content change over successive observation times) and WUD. The relationship between these variables and the WUD was tested for the non-leaching period (between 24 and 25 DaS). All the variables were normalized using the following equation.

$$\hat{Y}_i = \frac{Y_i}{\sum_{j=1}^{N} Y_j} \qquad \text{(Equation 3)}$$

where Y is the variable of interest (Gd-DTPA^{2-} accumulation, WD and cumulative WUD), $\hat{Y}$ the corresponding normalized variable. Gd-DTPA^{2-} accumulation is defined as the increase of Gd-DTPA^{2-} concentration over the considered period and the cumulative water uptake density represents the total amount of water taken up by roots in each voxel over a certain time lapse.

Accepted Manuscript

Downloaded from https://academic.oup.com/jxb/advance-article-abstract/doi/10.1093/jxb/erz060/5336523 by The University of British Columbia Library user on 19 February 2019

3 Results

3.1 Root system architecture and development

The fully grown root system (at 25 DaS) generated from the MRI scans is represented in Figure 1 together with the retrieved age distribution of the root segments. The total root length was 3.23 m at 25 DaS, which corresponds to a mean root growth of 0.17 cm day^{-1} (taking into account the respective time of appearance of each root tip). This total root length refers to root segments with a diameter greater than 200 µm, which could be detected by MRI. It appears that roots were mainly located in the upper part of the soil column (79% of the total root length was found between 0 and 3 cm depth). Three root orders could be identified (1=taproot, 2=lateral roots connected to the taproot and 3=secondary laterals) and contributed contrastingly to the total root system length: 2.4%, 27.6% and 70% for root orders 1, 2 and 3, respectively. Root order had no significant impact on the root elongation rate of root orders 2 and 3 (whose mean was respectively 0.16 cm day^{-1} and 0.17 cm day^{-1}) while the root elongation of the taproot was higher (0.43 cm day^{-1}). The average root diameters were significantly different between root orders varying between 0.045 cm (root order 3), 0.06 cm (root order 2) and 0.11 cm (taproot). This difference between taproot and laterals diameters justifies the chosen scheme of hydraulic properties, namely that K_x and k_r differ between the taproot and the laterals of all orders (see section 2.4). The mean root lengths vary between 0.8 cm, 2.4 cm and 7.7 cm for the 3rd, 2nd and 1st root orders, respectively. On average, lateral root density is 4.8 laterals per cm of taproot and 3.3 second order laterals per cm of lateral root.

3.2 Simulated vs observed tracer distributions

The best root hydraulic parameter set could accurately reproduce the tracer distribution as suggested qualitatively by the simulated and observed tracer concentration distributions (Figures 2B-C). Panels B-C of Figure 2 show more accumulation in the top part of the column, where most roots are located. In general, the model tends to smooth out the concentration patterns with less high concentration spots in the bottom part of the column.

A quantitative comparison can be performed with the help of correlation plots between the experimental (MRI) and the simulated (R-SWMS) Gd-$DTPA^{2-}$ 3D concentration distributions (Figure 2D) or 1D concentration profiles (Figure 2E). In general, one can see that the spreading of the differences between measured and simulated concentrations increases with tracer concentration. The optimal parameter set results in a RMSE of 1.75 mmol L^{-1} and a r^2 of 0.55 with a slope of 0.66 when a 3D voxel per voxel comparison is performed. These values might appear poor but one must keep in mind that the spatial resolution was high (0.5 cm voxel width) and that uncertainty exists on the exact location of the root

Accepted Manuscript

Downloaded from https://academic.oup.com/jxb/advance-article-abstract/doi/10.1093/jxb/erz060/5336523 by The University of British Columbia Library user on 19 February 2019

segments in the soil (due to the manual root reconstruction and hence hardly quantifiable) and the lack of spatial resolution for very fine roots (< 200 µm).

This lack of accuracy in the coregistration of the soil and the root system is confirmed by the fact that the RMSE and r^2 were improved respectively to 0.22 mmol L^{-1} and 0.98 when the tracer concentration was averaged horizontally (Figure 2E). In this case, the slope of the linear regression is close to unity, indicating that the 1D concentration profiles are almost perfectly reproduced by the model. Figure 3 emphasizes the good agreement between experimental and simulated Gd-DTPA^{2-} concentration at 25 DaS. Indeed, one can see that the relation between the mean tracer concentration and the distance to the nearest lateral root is similar in both cases. Moreover, the standard deviation of both experimental and simulated data are in the same range.

3.3 Sensitivity of simulated tracer distributions to root hydraulic properties

Response surfaces (logarithm of the RMSE between observed and simulated Gd-DTPA^{2-} concentration at 25 DaS, Eq. 2) around the global optimal root hydraulic parameter set are shown in Figure 4. The 3D (voxel to voxel comparison) RMSE in the close vicinity to the model optimum (i.e. when the parameters are disturbed from 1/8 to 8 times the optimum) are comprised between 1.75 mmol L^{-1} (minimal value corresponding to the optimal root hydraulic parameters) and 4.11 mmol L^{-1}. These values can be compared to the observed range of Gd-DTPA^{2-} concentrations at 25 DaS, varying from 0 to 15.6 mmol L^{-1} with a mean of 2.1 mmol L^{-1}. It is observed that hydraulic properties of the lateral roots (subscripts Ly and Lo) are much more sensitive parameters than those of the taproot (subscript T). Indeed, the RMSE is completely insensitive to k_{rT}, because irrespective of the value of k_{rT}, the taproot does not take up much water and thus does not impact solute accumulation distribution. Above a minimal threshold value, K_{xT} can be increased without impacting the RMSE value. In other words, there is a minimum value for K_{xT} (1 cm^4 hPa^{-1} day^{-1}, its optimum value) above which K_{xT} is insensitive, i.e. non limiting the water fluxes, and thus not affecting water uptake and the tracer accumulation.

These response surfaces also allow us to visualize correlations that exist between parameters and hence model parameter trade-offs. k_{rLo} and k_{rLy} are positively correlated (if k_{rLy} is decreased, then k_{rLo} should be decreased as well to maintain model performance); k_{rLy} and K_{xLy} are negatively correlated (an increase/decrease of k_{rLy} combined with a decrease/increase of $K_{x,y}$ will not influence the modeled concentration); the same observation can be made for K_{xLo} and K_{xLy}. These correlations between root hydraulic parameters express how similar Gd-DTPA^{2-} accumulation distribution around roots can be obtained from different root hydraulic properties. First, the same distributions of uptake along a root can be obtained when the radial conductivities of young and old segments are simultaneously decreased. On the other hand, to maintain the same uptake from young segments, their axial conductance should increase

Accepted Manuscript

Downloaded from https://academic.oup.com/jxb/advance-article-abstract/doi/10.1093/jxb/erz060/5336523 by The University of British Columbia Library user on 19 February 2019

when their radial conductivity is decreased. But, when the axial conductance of the younger segments is increased, the axial conductance of the older segments should be decreased so that the uptake is not shifted towards the younger root segments. These examples show how the correlations between root hydraulic parameters can be related to the hydraulics of single roots (Landsberg & Fowkes. 1978; Meunier et al. 2017). Figure S2 shows the sensitivity of water uptake density to root hydraulic properties.

The sensitivity analysis (Figure 4) pointed out that the tracer distribution is more impacted by radial conductivities than axial conductances. This implies that, in our case, k_r is more limiting than K_x for water uptake, which is in agreement with the results of Frensch & Steudle (1989). A change of k_{rLy} or k_{rLo} increases significantly the RMSE (Figure 4). In fact, if k_{rLo} gets higher, this implies that RWU partitioning between young and old root segments will change; old root segments will take more water and young ones will take less than in the optimal scenario. In the specific case where k_{rLo} is multiplied by 6 ($6*10^{-3}$ cm hPa^{-1} day^{-1}) and k_{rLy} is divided by 2 ($5*10^{-3}$ cm hPa^{-1} day^{-1}), all lateral root segments have the same ability to take up water from the soil. The larger RSME for this scenario (see Figure 4) leads us to affirm that the oldest root segments (> 5 days-old) should not be able to take water at a same or higher rate than the youngest one. This validates our original assumption that k_r decreases with root maturation (i.e. root aging). To further demonstrate the impact of root hydraulics (and hence root water uptake) distribution on tracer concentration, we also compared the tracer distributions resulting from a scenario in which the taproot is the main location of water uptake and from the optimal scenario (see Video S1).

3.4 Optimized root hydraulic parameters

In Figure 5, we compare our optimal root hydraulic parameter set with the ones of Doussan et al. (2006); Bramley et al. (2007); Zarebanadkouki et al. (2016) and Meunier et al. (2018a), who all worked on lupine plants. One can see that K_x is higher in the taproot than in the lateral roots whereas the opposite tendency is observed for k_r. Another observation is that, for lateral roots, K_x increases with root age. As explained earlier, we imposed a decreasing k_r with root age but K_x was not subject to any constraint. The maturation of xylem vessels in the early development stages could explain that K_x increases with root development (Vetterlein & Doussan 2016). The root radial conductivities found in this study span 2 orders of magnitude between the youngest and the oldest root segments. The root axial conductances of the different roots orders and ages retrieved by inverse modeling for the considered RSA cover 4 orders of magnitude. One should notice that the taproot axial conductance (K_{xT}=1 cm^4 hPa^{-1} day^{-1}) corresponds to the upper limit of the considered parametric space. Moreover, as shown in Figure 4, the K_{xT} value found represents the lower bound of conductances that could represent the tracer distribution. However, the taproot axial conductance found is larger and its radial conductivity is smaller than in previous experiments performed on lupine. Considering lateral root segments of the same age, the axial conductance value is close to the values found in the

Accepted Manuscript

Downloaded from https://academic.oup.com/jxb/advance-article-abstract/doi/10.1093/jxb/erz060/5336523 by The University of British Columbia Library user on 19 February 2019

published literature for K_{xLy} but not for K_{xLo}. The radial conductivity retrieved by optimization for the young (k_{rLy}) and the old root segments (k_{rLo}) are comprised in the same ranges than the previously cited literature.

An alternative way to assess the reliability of the determined root hydraulic properties is to check the root system total hydraulic conductivity (k_{rs}, also L_{pr} in literature). k_{rs} is the root system total hydraulic conductance (K_{rs}) divided by the total root surface. Bramley et al. (2009) measured it on a 14-day-old lupine plant (k_{rs}=1.31*10^{-7} m MPa^{-1} s^{-1}). Our results (k_{rs}=1.63*10^{-6} m MPa^{-1} s^{-1} for a 25-day-old root system; k_{rs}=3.8*10^{-7} m MPa^{-1} s^{-1} for a 14-day-old root system) suggest a good agreement and support the plausibility of the determined root hydraulic properties.

3.5 Inter- and extrapolations

In a second step, we used these optimal root hydraulic properties to simulate the whole experiment (from 18 to 25 DaS). The simulated 1D vertical profiles of Gd-DTPA^{2-} concentrations are presented together with the experimental profiles (MRI) in Figure 6A. The corresponding determination coefficients are high (covering a range from 0.74 to 0.99), especially for the first two days of the experiment (r^2=0.99 and r^2=0.91). However, after two days, one can observe a mismatch between simulated and observed profiles, especially for the lower part of the soil column (deeper than 4 cm). At the end of the experiment (at 25 DaS), the observed and modeled concentration profiles have the same shape (and so the correlation is good) but the absolute concentration values are different. This discrepancy is also visible in the breakthrough curve simulation, which clearly lag behind the observed data (Figure 6B). This is likely due to some preferential flow paths occurring at depths lower than 4 cm. Indeed, simulations show that the tracer front is slowly moving downwards (i.e. the front is flat) whereas MRI-derived Gd-DTPA^{2-} reaches the bottom of the soil column much quicker in the experiment. The difference in tracer concentration at 25 DaS is due to a higher tracer mass in the modeled soil column than in the experimental one. Indeed, since tracer particles reach the column bottom later, there were less tracer mass in the effluent and more were left in soil column. Further optimization of the soil conductivity parameters for that part of the soil profile (e.g. taking into account the soil heterogeneities) could have improved the fitting but was beyond the scope of this paper. Despite the fact that the observed breakthrough curve could not be properly modeled when starting the simulation at 18 DaS, we assumed that the root hydraulic parameters were right as (i) they are very sensitive to the second step of the experiment and not to the first part, (ii) this preferential flow is related to soil parameterization rather than root properties, and (iii) the impact of the preferential flow on the mass balance of the tracer in the soil profile was accounted for by setting the initial conditions of the concentrations at the last moment of the leaching phase for which concentration map was available (at 23 DaS, the end of the leaching phase is at 24 DaS) based on the MRI measured concentration distributions (see 25 DaS* in Figure 6A).

Accepted Manuscript

Downloaded from https://academic.oup.com/jxb/advance-article-abstract/doi/10.1093/jxb/erz060/5336523 by The University of British Columbia Library user on 19 February 2019

3.6 Determining RWU distributions

We can use the optimal parameter set to access not directly observable variables of the SPAC, such as RWU distribution. Figure 7 shows the total cumulative water uptake over the whole experiment (from 18 to 25 DaS) in cm^3. We can see that water is mainly taken up by lateral roots (76% by third order root segments, 23% by second order ones and barely 1% by the taproot). This is in agreement with Zarebanadkouki et al. (2016) who also found out that soil water was mainly taken up by lateral roots in lupine plant. We can also observe (i) an increase in the uptake rate between the first and the last day of the experiment, which is a consequence of the doubling of lupine transpiration rate during this period (see Table S1), (ii) that water was mostly taken close to the root tip, corresponding to a zone with young root segments with high radial conductivity and a conductive enough axial conductance and (iii) that water was taken over the whole rooting depth both under wetter (at 19 DaS) and dryer (at 25 DaS) conditions. This indicates that soil hydraulic conductivity was not limiting RWU, even under the relatively drier conditions. The mean water content and mean soil water potential (h) at 19 DaS and at 25 DaS are θ_{19}=0.36, h_{19}=-1.86*10^{-3} MPa, θ_{25}=0.21, and h_{25}=-3.53*10^{-3} MPa, respectively (see Figure S3).

In Figure 8, we evaluate the relation between two proxies, the water depletion and the tracer accumulation, and the WUD during the non-leaching period. From these plots, it is obvious that water depletion does not reflect the cumulative WUD appropriately. Gd-$DTPA^{2-}$ accumulation gives an accurate view of the cumulative WUD in 1D (r^2=0.91). However, its accuracy to predict 3D cumulative WUD distribution is less evident and highly dependent on the considered spatial resolution. The proxies displayed in Figure 8 are the results averaged to a mean voxel size of 0.5 cm.

Accepted Manuscript

Downloaded from https://academic.oup.com/jxb/advance-article-abstract/doi/10.1093/jxb/erz060/5336523 by The University of British Columbia Library user on 19 February 2019

4 Discussion

4.1 Tracer accumulation

The potential of an experiment using a plant-excluded tracer to retrieve quantitative information on root hydraulics was assessed by fitting the 3D concentration built up around roots during a no irrigation phase with a process-based model of the soil-root continuum. The simulated and observed high concentrations are similarly located, but their actual values might differ. A possible explanation could be that, for high concentration (> 5 mmol L^{-1}), the uncertainty range of the MRI measured concentrations becomes higher (see Figure 7 in Haber-Pohlmeier et al. (2017)).

4.2 Proxies for WUD

The poor correlation between WD and WUD in model simulations supports the exclusion of the former as a suitable proxy for WUD. During non-leaching phase, the 3D local tracer accumulation is a much better proxy for the WUD than the WD but still, considerable noise on the relation between local WUD and tracer accumulation exists and this noise increases with increasing spatial resolution. As shown in Figure 9, Gd-$DTPA^{2-}$ accumulation seems to be influenced not only by the local cumulative WUD but also by the neighbouring concentrations (or neighbouring uptake). For example, a voxel that is subject to a small WUD and that is located next to a voxel in which water is intensely taken up may experience an important Gd-$DTPA^{2-}$ accumulation since the tracer is exponentially distributed around the water uptake sink (Figure 3). Moreover, one should keep in mind that Gd-$DTPA^{2-}$ redistribution took place only during one day after the leaching phase. One could expect better correlations with longer redistribution periods.

4.3 Validation of a FSRSM

The fact that the FSRSM could reproduce the observed tracer distribution when the root hydraulic parameters were calibrated could be considered as an indirect validation of the FSRSM. Indeed, the values of the optimized parameters were in agreement with what is expected based on root anatomy and were in accordance with values from previous studies of the same species. We demonstrated how a calibrated and validated FSRSM could be applied to assess water uptake by different root orders and at different locations along a single root.

4.4 Opportunities

Accepted Manuscript

Downloaded from https://academic.oup.com/jxb/advance-article-abstract/doi/10.1093/jxb/erz060/5336523 by The University of British Columbia Library user on 19 February 2019

Nowadays selection of drought tolerant genotypes is often based on structural traits such as rooting depth, root length density or RSA (de Dorlodot et al. 2007; Trachsel et al. 2010; Paez-Garcia et al. 2015) but local root hydraulic properties are also crucial (Vadez 2014).

A validated FSRSM can be used to quantify the impact of a combination of root structural and functional traits on root water uptake (Meunier et al. 2017). Coupled with an entire plant model, FSRSM allow us to determine ideotypes for RWU (Leitner et al. 2014; van Eeuwijk et al. 2018).

Moreover, the use of FSRSMs in inverse modeling scheme opens new avenues to translate information that is obtained from sophisticated tracer experimental methods into information that can be used for practical applications (e.g. retrieve the root hydraulic properties *in situ*). Although this study demonstrated the unique capability of MRI to image root architectures and tracer distributions, there is still a far way to go before this method can be used as standardized and high-throughput method for root hydraulic phenotyping.

Another application of FSRSM is the retrieval of root hydraulic characteristics with methods based on the isotopic composition of water (e.g. Meunier et al. 2018b).

5 Conclusion

This study is the first that combines 4D (space and time) RSA with spatially resolved measurements of root zone tracer concentrations to validate/parameterize a FSRSM. We showed that R-SWMS, a FSRSM, can properly represent water and solute fluxes in the root zone. Moreover, 3D tracer distribution maps were proven to contain valuable information to infer hydraulic parameters of roots of different orders and ages. The retrieved parameter set was in the range of other studies of lupine plants. The use of the model also allowed us to unravel the RWU dynamics *in situ*. RWU was shown to be affected by root growth and in particular by the root age distribution, which affected the root hydraulic architecture. The 3rd order roots, which represented 70% of the total root length, extracted 76% of water. The simulations highlighted that water content changes or tracer accumulation were not suitable proxies for water uptake. The validation of such models opens new opportunities for developing drought tolerant ideotype.

Accepted Manuscript

Downloaded from https://academic.oup.com/jxb/advance-article-abstract/doi/10.1093/jxb/erz060/5336523 by The University of British Columbia Library user on 19 February 2019

Acknowledgements

During the preparation of this manuscript, F.M. was supported by "Fonds National de la Recherche Scientifique" of Belgium (FNRS) as Research Fellow and is grateful to this fund for its support. This work was also supported by the Belgian French community ARC 16/21-075 project.

Accepted Manuscript

Downloaded from https://academic.oup.com/jxb/advance-article-abstract/doi/10.1093/jxb/erz060/5336523 by The University of British Columbia Library user on 19 February 2019

6 References

Ahmed, M. A., M. Zarebanadkouki, A. Kaestner, and A. Carminati. 2015. "Measurements of Water Uptake of Maize Roots: The Key Function of Lateral Roots." *Plant and Soil* 398 (1-2): 59–77.

Bechtold, M., J. Vanderborght, O. Ippisch, and H. Vereecken. 2011. "Efficient Random Walk Particle Tracking Algorithm for Advective-Dispersive Transport in Media with Discontinuous Dispersion Coefficients and Water Contents." *Water Resources Research* 47 (10). https://doi.org/10.1029/2010wr010267.

Bodner, G., M. Alsalem, A. Nakhforoosh, T. Arnold, and D. Leitner. 2017. "RGB and Spectral Root Imaging for Plant Phenotyping and Physiological Research: Experimental Setup and Imaging Protocols." *Journal of Visualized Experiments: JoVE*, no. 126 (August). https://doi.org/10.3791/56251.

Bramley, H., N. C. Turner, D. W. Turner, and S. D. Tyerman. 2007. "Comparison between Gradient-Dependent Hydraulic Conductivities of Roots Using the Root Pressure Probe: The Role of Pressure Propagations and Implications for the Relative Roles of Parallel Radial Pathways." *Plant, Cell & Environment* 30 (7): 861–74.

Bramley, H., N. C. Turner, D. W. Turner, and S. D. Tyerman. 2009. "Roles of Morphology, Anatomy, and Aquaporins in Determining Contrasting Hydraulic Behavior of Roots." *Plant Physiology* 150 (1): 348–64.

Carminati, A., A. B. Moradi, D. Vetterlein, P. Vontobel, E. Lehmann, U. Weller, H. J. Vogel, and S. E. Oswald. 2010. "Dynamics of Soil Water Content in the Rhizosphere." *Plant and Soil* 332 (1-2): 163–76.

de Dorlodot, S., B. Forster, L. Pagès, A. Price, R. Tuberosa, and X. Draye. 2007. "Root System Architecture: Opportunities and Constraints for Genetic Improvement of Crops." *Trends in Plant Science* 12 (10): 474–81.

Diggle, A. J. 1988. "Rootmap: A Root Growth Model." *Mathematics and Computers in Simulation* 30 (1-2): 175–80.

Doussan, C., A. Pierret, E. Garrigues, and L. Pagès. 2006. "Water Uptake by Plant Roots: II – Modelling of Water Transfer in the Soil Root-System with Explicit Account of Flow within the Root System – Comparison with Experiments." *Plant and Soil* 283 (1-2): 99–117.

Dunbabin, V., Z. Rengel, and A. J. Diggle. 2004. "Simulating Form and Function of Root Systems: Efficiency of Nitrate Uptake Is Dependent on Root System Architecture and the Spatial and Temporal Variability of Nitrate Supply." *Functional Ecology* 18 (2): 204–11.

Esser, H. G., A. Carminati, P. Vontobel, E. H. Lehmann, and S. E. Oswald. 2010. "Neutron Radiography and Tomography of Water Distribution in the Root Zone." *Journal of Plant Nutrition and Soil Science* 173 (5): 757–64.

Frensch, J., and E. Steudle. 1989. "Axial and Radial Hydraulic Resistance to Roots of Maize (Zea Mays L.)." *Plant Physiology* 91 (2): 719–26.

Haber-Pohlmeier, S., M. Bechtold, S. Stapf, and A. Pohlmeier. 2010. "Water Flow Monitored by Tracer Transport in Natural Porous Media Using Magnetic Resonance Imaging." *Vadose Zone Journal* 9 (4): 835.

Haber-Pohlmeier, S., J. Vanderborght, and A. Pohlmeier. 2017. "Quantitative Mapping of Solute

Accepted Manuscript

Downloaded from https://academic.oup.com/jxb/advance-article-abstract/doi/10.1093/jxb/erz060/5336523 by The University of British Columbia Library user on 19 February 2019

Accumulation in a Soil-Root System by Magnetic Resonance Imaging." *Water Resources Research* 53 (8): 7469–80.

Hachez, Charles, Dmitry Veselov, Qing Ye, Hagen Reinhardt, Thorsten Knipfer, Wieland Fricke, and François Chaumont. 2012. "Short-Term Control of Maize Cell and Root Water Permeability through Plasma Membrane Aquaporin Isoforms." *Plant, Cell & Environment* 35 (1): 185–98.

Hainsworth, J. M., and L. Aylmore. 1983. "The Use of Computer Assisted Tomography to Determine Spatial Distribution of Soil Water Content." *Australian Journal of Soil Research* 21 (4): 435.

Javaux, M., T. Schröder, J. Vanderborght, and H. Vereecken. 2008. "Use of a Three-Dimensional Detailed Modeling Approach for Predicting Root Water Uptake." *Vadose Zone Journal* 7 (3): 1079.

Jorda, H., A. Perelman, N. Lazarovitch, and J. Vanderborght. 2018. "Exploring Osmotic Stress and Differences between Soil–Root Interface and Bulk Salinities." *Vadose Zone Journal* 17 (1): 0.

Koebernick, N., K. Huber, E. Kerkhofs, J. Vanderborght, M. Javaux, H. Vereecken, and D. Vetterlein. 2015. "Unraveling the Hydrodynamics of Split Root Water Uptake Experiments Using CT Scanned Root Architectures and Three Dimensional Flow Simulations." *Frontiers in Plant Science* 6 (May): 370.

Koebernick, N., U. Weller, K. Huber, S. Schlüter, H. J. Vogel, R. Jahn, H. Vereecken, and D. Vetterlein. 2014. "In Situ Visualization and Quantification of Three-Dimensional Root System Architecture and Growth Using X-Ray Computed Tomography." *Vadose Zone Journal* 13 (8): 0.

Landl, Magdalena, Katrin Huber, Andrea Schnepf, Jan Vanderborght, Mathieu Javaux, A. Glyn Bengough, and Harry Vereecken. 2016. "A New Model for Root Growth in Soil with Macropores." *Plant and Soil* 415 (1-2): 99–116.

Landsberg, J. J., and N. D. Fowkes. 1978. "Water Movement Through Plant Roots." *Annals of Botany* 42 (3): 493–508.

Leitner, D., F. Meunier, G. Bodner, M. Javaux, and A. Schnepf. 2014. "Impact of Contrasted Maize Root Traits at Flowering on Water Stress Tolerance – A Simulation Study." *Field Crops Research* 165: 125–37.

Leitner, D., A. Schnepf, S. Klepsch, and T. Roose. 2010. "Comparison of Nutrient Uptake between Three-dimensional Simulation and an Averaged Root System Model." *Plant Biosystems - An International Journal Dealing with All Aspects of Plant Biology* 144 (2): 443–47.

Li, Q.M., and B.B. Liu. 2010. "Comparison of Three Methods for Determination of Root Hydraulic Conductivity of Maize (Zea Mays L.) Root System." *Agricultural Sciences in China / Sponsored by the Chinese Academy of Agricultural Sciences* 9 (10): 1438–47.

Li, S., X. Liu, M. Wang, and L. He. 2015. "Analyzing Root Plasticity to Phosphorus with a Three Dimensional Architectural Model." *Journal of Computational and Theoretical Nanoscience* 12 (12): 6044–50.

Li, S., X. Liu, M. Wang, and W. Yu. 2016. "Exploring Root Plasticity to Resource Patches Based on Swarm Behavior." *Acta Physiologiae Plantarum / Polish Academy of Sciences, Committee of Plant Physiology Genetics and Breeding* 38 (8). https://doi.org/10.1007/s11738-016-2227-2.

Mairhofer, S., S. Zappala, S. R. Tracy, C. Sturrock, M. Bennett, S. J. Mooney, and T. Pridmore. 2012.

Accepted Manuscript

Downloaded from https://academic.oup.com/jxb/advance-article-abstract/doi/10.1093/jxb/erz060/5336523 by The University of British Columbia Library user on 19 February 2019

"RooTrak: Automated Recovery of Three-Dimensional Plant Root Architecture in Soil from X-Ray Microcomputed Tomography Images Using Visual Tracking." *Plant Physiology* 158 (2): 561–69.

Meunier, F., V. Couvreur, X. Draye, J. Vanderborght, and M. Javaux. 2017. "Towards Quantitative Root Hydraulic Phenotyping: Novel Mathematical Functions to Calculate Plant-Scale Hydraulic Parameters from Root System Functional and Structural Traits." *Journal of Mathematical Biology* 75 (5): 1133–70.

Meunier, F., M. Javaux, V. Couvreur, X. Draye, and J. Vanderborght. 2016. "A New Model for Optimizing the Water Acquisition of Root Hydraulic Architectures over Full Crop Cycles." In *2016 IEEE International Conference on Functional-Structural Plant Growth Modeling, Simulation, Visualization and Applications (FSPMA)*. https://doi.org/10.1109/fspma.2016.7818300.

Meunier, F., M. Zarebanadkouki, M. A. Ahmed, A. Carminati, V. Couvreur, and M. Javaux. 2018a. "Hydraulic Conductivity of Soil-Grown Lupine and Maize Unbranched Roots and Maize Root-Shoot Junctions." *Journal of Plant Physiology*, January. https://doi.org/10.1016/j.jplph.2017.12.019.

Meunier, F., Y. Rothfuss, T. Bariac, P. Biron, P. Richard, JL Durand, V. Couvreur, J. Vanderborght, and M. Javaux. 2018b. "Measuring and Modeling Hydraulic Lift of Using Stable Water Isotopes." *Vadose Zone Journal* 17 (1): 0.

Moradi, A. B., A. Carminati, D. Vetterlein, P. Vontobel, E. Lehmann, U. Weller, J. W. Hopmans, H-J Vogel, and S. E. Oswald. 2011. "Three-Dimensional Visualization and Quantification of Water Content in the Rhizosphere." *The New Phytologist* 192 (3): 653–63.

Mualem, Y. 1976. "A New Model for Predicting the Hydraulic Conductivity of Unsaturated Porous Media." *Water Resources Research* 12 (3): 513–22.

Ndour, A., V. Vadez, C. Pradal, and M. Lucas. 2017. "Virtual Plants Need Water Too: Functional-Structural Root System Models in the Context of Drought Tolerance Breeding." *Frontiers in Plant Science* 8 (September): 1577.

Paez-Garcia, A., C. M. Motes, W.-R. Scheible, R. Chen, E. B. Blancaflor, and M. J. Monteros. 2015. "Root Traits and Phenotyping Strategies for Plant Improvement." *Plants* 4 (2): 334–55.

Passot, Sixtine, Valentin Couvreur, Félicien Meunier, Xavier Draye, Mathieu Javaux, Daniel Leitner, Loïc Pagès, Andrea Schnepf, Jan Vanderborght, and Guillaume Lobet. 2018. "Connecting the Dots between Computational Tools to Analyse Soil-Root Water Relations." *Journal of Experimental Botany*, October. https://doi.org/10.1093/jxb/ery361.

Pohlmeier, A. 2010. "MRI in Soils: Determination of Water Content Changes Due to Root Water Uptake by Means of a Multi-Slice-Multi-Echo Sequence (MSME)." *The Open Magnetic Resonance Journal* 3 (1): 69–74.

Postma, J. A., and J. P. Lynch. 2012. "Complementarity in Root Architecture for Nutrient Uptake in Ancient Maize/bean and Maize/bean/squash Polycultures." *Annals of Botany* 110 (2): 521–34.

Rieger, M., and P. Litvin. 1999. "Root System Hydraulic Conductivity in Species with Contrasting Root Anatomy." *Journal of Experimental Botany* 50 (331): 201–9.

Schnepf, A., D. Leitner, M. Landl, G. Lobet, T. H. Mai, S. Morandage, C. Sheng, M. Zörner, J. Vanderborght, and H. Vereecken. 2018. "CRootBox: A Structural-Functional Modelling Framework for Root Systems."

Accepted Manuscript

Downloaded from https://academic.oup.com/jxb/advance-article-abstract/doi/10.1093/jxb/erz060/5336523 by The University of British Columbia Library user on 19 February 2019

Annals of Botany 121 (5): 1033–53.

Schröder, N. 2014. *Three-Dimensional Solute Transport Modeling in Coupled Soil and Plant Root Systems*. Forschungszentrum Jülich.

Schröder, N, M. Javaux, J. Vanderborght, B. Steffen, and H. Vereecken. 2012. "Effect of Root Water and Solute Uptake on Apparent Soil Dispersivity: A Simulation Study." *Vadose Zone Journal* 11 (3): 0.

Schröder, N., N. Lazarovitch, J. Vanderborght, H. Vereecken, and M. Javaux. 2013. "Linking Transpiration Reduction to Rhizosphere Salinity Using a 3D Coupled Soil-Plant Model." *Plant and Soil* 377 (1-2): 277–93.

Schwartz, N., A. Carminati, and M. Javaux. 2016. "The Impact of Mucilage on Root Water Uptake-A Numerical Study." *Water Resources Research* 52 (1): 264–77.

Stingaciu, L., H. Schulz, A. Pohlmeier, S. Behnke, H. Zilken, M. Javaux, and H. Vereecken. 2013. "In Situ Root System Architecture Extraction from Magnetic Resonance Imaging for Water Uptake Modeling." *Vadose Zone Journal* 0 (0): 0.

Strock, C. F., L. Morrow de la Riva, and J. P. Lynch. 2018. "Reduction in Root Secondary Growth as a Strategy for Phosphorus Acquisition." *Plant Physiology* 176 (1): 691–703.

Tötzke, C., N. Kardjilov, I. Manke, and S. E. Oswald. 2017. "Capturing 3D Water Flow in Rooted Soil by Ultra-Fast Neutron Tomography." *Scientific Reports* 7 (1): 6192.

Trachsel, S., S. M. Kaeppler, K. M. Brown, and J. P. Lynch. 2010. "Shovelomics: High Throughput Phenotyping of Maize (Zea Mays L.) Root Architecture in the Field." *Plant and Soil* 341 (1-2): 75–87.

van Eeuwijk, F. A., D. Bustos-Korts, E. J. Millet, M. P. Boer, W. Kruijer, A. Thompson, M. Malosetti, et al. 2018. "Modelling Strategies for Assessing and Increasing the Effectiveness of New Phenotyping Techniques in Plant Breeding." *Plant Science: An International Journal of Experimental Plant Biology*. https://doi.org/10.1016/j.plantsci.2018.06.018.

van Genuchten, M. T. 1980. "A Closed-Form Equation for Predicting the Hydraulic Conductivity of Unsaturated Soils." *Soil Science Society of America Journal. Soil Science Society of America* 44 (5): 892.

Vadez, V. 2014. "Root Hydraulics: The Forgotten Side of Roots in Drought Adaptation." *Field Crops Research* 165: 15–24.

Vandoorne, B., L. Beff, S. Lutts, and M. Javaux. 2012. "Root Water Uptake Dynamics of Var. Under Water-Limited Conditions." *Vadose Zone Journal* 11 (3): 0.

Vetterlein, D., and C. Doussan. 2016. "Root Age Distribution: How Does It Matter in Plant Processes? A Focus on Water Uptake." *Plant and Soil* 407 (1-2): 145–60.

Zarebanadkouki, M., Y. X. Kim, and A. Carminati. 2013. "Where Do Roots Take up Water? Neutron Radiography of Water Flow into the Roots of Transpiring Plants Growing in Soil." *The New Phytologist* 199 (4): 1034–44.

Zarebanadkouki, M., Y. X. Kim, A. B. Moradi, H-J Vogel, A. Kaestner, and A. Carminati. 2012. "Quantification and Modeling of Local Root Water Uptake Using Neutron Radiography and Deuterated

Accepted Manuscript

Downloaded from https://academic.oup.com/jxb/advance-article-abstract/doi/10.1093/jxb/erz060/5336523 by The University of British Columbia Library user on 19 February 2019

Water." *Vadose Zone Journal* 11 (3): 0.

Zarebanadkouki, M., E. Kroener, A. Kaestner, and A. Carminati. 2014. "Visualization of Root Water Uptake: Quantification of Deuterated Water Transport in Roots Using Neutron Radiography and Numerical Modeling." *Plant Physiology* 166 (2): 487–99.

Zarebanadkouki, M., F. Meunier, V. Couvreur, J. Cesar, M. Javaux, and A. Carminati. 2016. "Estimation of the Hydraulic Conductivities of Lupine Roots by Inverse Modelling of High-Resolution Measurements of Root Water Uptake." *Annals of Botany*, August. https://doi.org/10.1093/aob/mcw154.

Accepted Manuscript

Downloaded from https://academic.oup.com/jxb/advance-article-abstract/doi/10.1093/jxb/erz060/5336523 by The University of British Columbia Library user on 19 February 2019

Figure captions

Figure 1. Schematics of the experimental set-up. The experimental column and the reconstructed final (at 25 DaS) root architecture are shown. The fluxes considered in the modeling are irrigation (I), transpiration (T), and effluent (E). The experimental and simulated column cross sections are also shown.

Figure 2. Panel A: 3D tracer concentration distribution at 23 DaS , imaged by MRI and used as initial condition for the model. Panel B: Tracer concentration distribution measured by MRI at 25 DaS. Panel C: Tracer concentration distribution modeled by R-SWMS at 25 DaS. Panel D: Correlation between experimental (MRI) and simulated (R-SWMS) final (at 25 DaS) 3D tracer concentration distributions (mmol L^{-1}). Panel E: Correlation between experimental (MRI) and simulated (R-SWMS) final (at 25 DaS) horizontally-averaged concentration distributions (mmol L^{-1}) with horizontal and vertical error bars representing the observed and simulated standard deviations at each depth, respectively

Figure 3. Gd-$DTPA^{2-}$ concentration (mmol L^{-1}) in a voxel vs. distance to the nearest lateral root at 25 DaS. The voxels were binned with a interval of 0.25 cm The solid lines represent the mean concentration and the shaded areas cover ± one standard deviation.

Figure 4. RMSE (mmol L^{-1}) between observed and simulated Gd-$DTPA^{2-}$ concentrations at 25 DaS as a function of root hydraulic property values considered in the simulations. The lower the RMSE (i.e. the lighter in the figure), the closer the simulation results to the experimental ones. The black crosses correspond to the lowest RMSE, and to the optimal parameter sets. The corresponding optimal parameters are given for each plot. K_x and k_r are in cm^4 hPa^{-1} day^{-1} and cm hPa^{-1} day^{-1}, respectively. The subscripts T, Ly and Lo refer to taproot, young laterals and old laterals, respectively.

Figure 5. Panels A and B: Comparison of optimized radial conductivities (k_r) and axial conductances (K_x) with existing literature values for lupine plants. The hydraulic properties of the taproot are assigned by the subscript T and those of the lateral roots by the subscripts Ly and Lo for the young (0-5 days old) and the old root segments (5-25 days old), respectively. The best root hydraulic properties in this study are represented as black dots. The grey envelopes stand for the ranges of root hydraulic properties values covered by Doussan et al. (2006), Bramley et al. (2007), Zarebanadkouki et al. (2016) and Meunier et al. (2018a). Panel C: Root system architecture at 25 DaS.

Figure 6. Panel A: Modeled (solid lines for simulation from 18 to 25 DaS and dotted line for simulation from 23 to 25 DaS) and measured (+) Gd-$DTPA^{2-}$ concentration profiles (mmol L^{-1}). Panel B: Modeled (blue stars) and measured (black stars) breakthrough curves. The horizontal black line in panel B represents the Gd-$DTPA^{2-}$ concentration (mmol L^{-1}) of the irrigation solution, constant over the entire experiment.

Accepted Manuscript

Downloaded from https://academic.oup.com/jxb/advance-article-abstract/doi/10.1093/jxb/erz060/5336523 by The University of British Columbia Library user on 19 February 2019

Figure 7. Panel A: Line graph of the cumulative root water uptake volume (cm^3) by root order throughout the whole experiment and pie chart of water uptake contribution by root order (at 25 DaS). Panel B: Radial root flow distributions over a day ($cm^3\ cm^{-2}\ day^{-1}$) during the first (left, at 19 DaS) and the last (right, at 25 DaS) day of the experiment. Water uptake density 1D profiles are also given (black lines).

Figure 8. Panel A: Correlations between 3D water depletion (WD in $cm^3\ cm^{-3}$), 3D Gd-$DTPA^{2-}$ accumulation (Acc. in mmol L^{-1}), and 3D cumulative water uptake density (WUD) for a voxel size of 0.5 cm (in $cm^3\ cm^{-3}\ day^{-1}$). Panel B: 1D vertical profiles of WD, Acc. and WUD over 1 day (from 24 to 25 DaS). WD states for the change of water content; Acc. represents the increase of tracer concentration and the cumulative WUD is the total amount of water taken by roots in each voxel. In panel A, the identity line is represented in black. The correlations were analyzed during the non-leaching period only (from 24 to 25 DaS).

Figure 9. 3D distribution of water depletion (WD in $cm^3\ cm^{-3}$), Gd-$DTPA^{2-}$ accumulation (Acc. in mmol L^{-1}) and cumulative water uptake density (WUD in $cm^3\ cm^{-3}\ day^{-1}$) for the optimal root hydraulic properties. WD states for the variation of water content; Acc. represents the increase of tracer concentration. Cumulative WUD, WD and solute accumulation are considered between 24 and 25 DaS only (non leaching phase only).

Accepted Manuscript

Downloaded from https://academic.oup.com/jxb/advance-article-abstract/doi/10.1093/jxb/erz060/5336523 by The University of British Columbia Library user on 19 February 2019

Figures

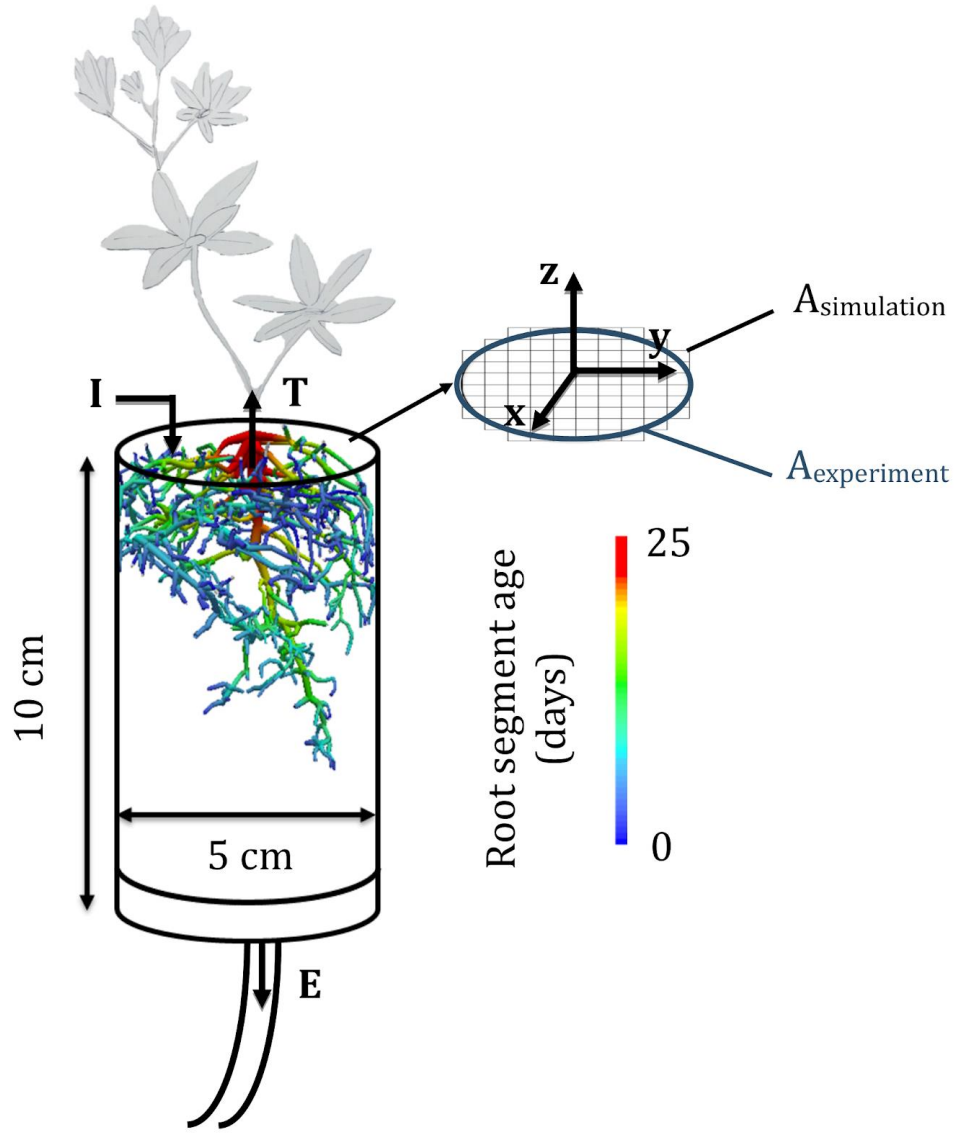

Figure 1

Color online, not print

Downloaded from https://academic.oup.com/jxb/advance-article-abstract/doi/10.1093/jxb/erz060/5336523 by The University of British Columbia Library user on 19 February 2019

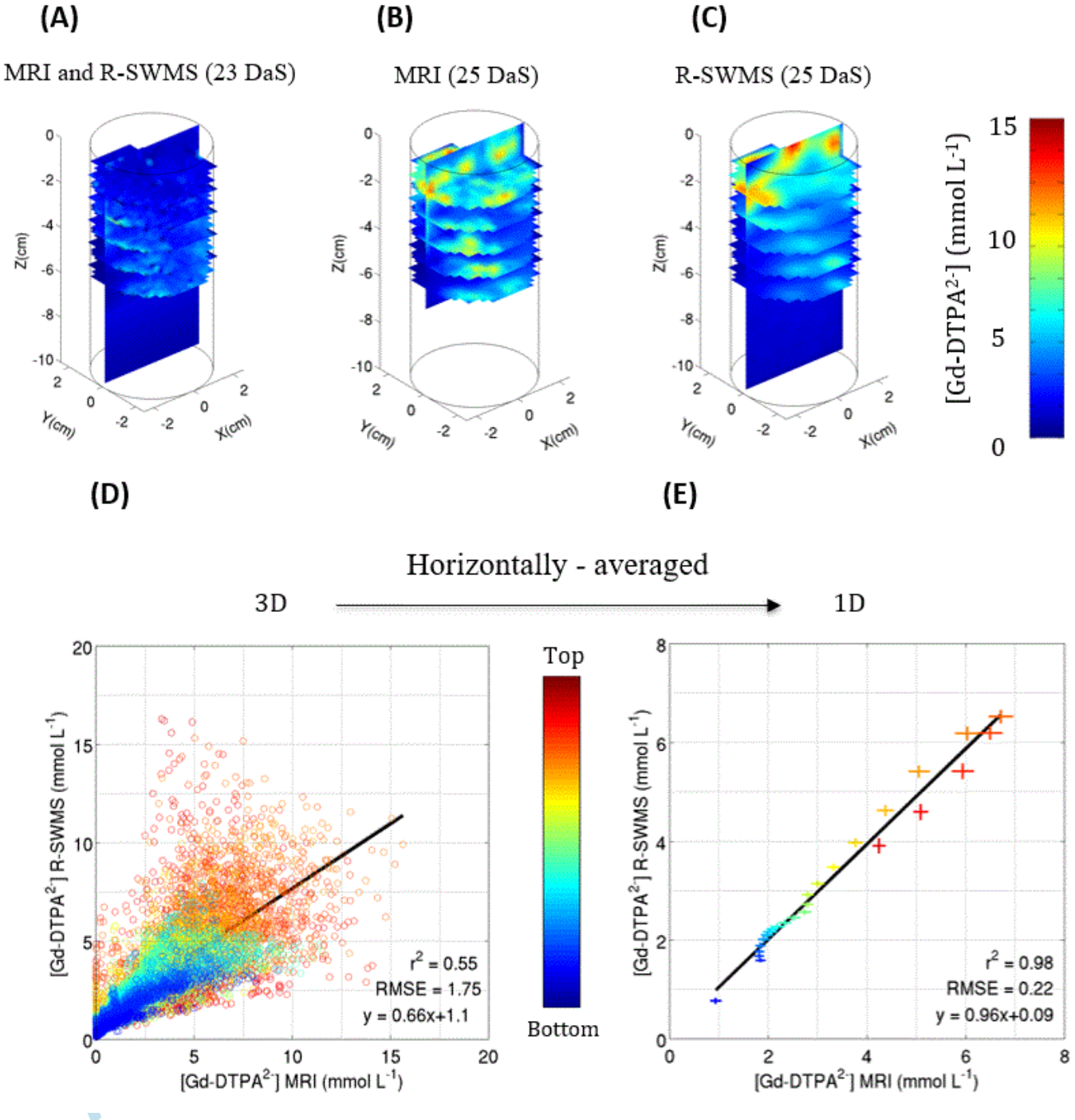

Figure 2

Color online, not print

Downloaded from https://academic.oup.com/jxb/advance-article-abstract/doi/10.1093/jxb/erz060/5336523 by The University of British Columbia Library user on 19 February 2019

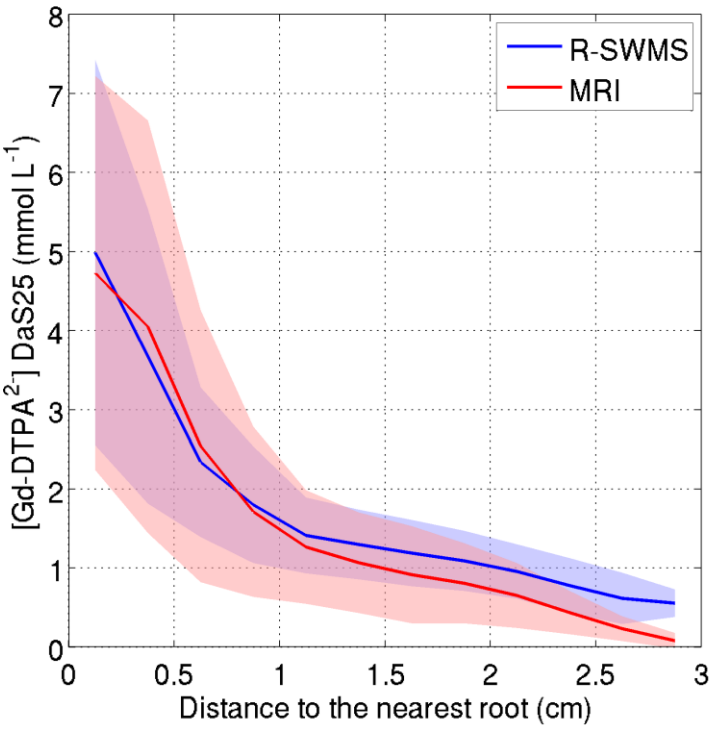

Figure 3

Color online, not print

Accepted Manuscript

Downloaded from https://academic.oup.com/jxb/advance-article-abstract/doi/10.1093/jxb/erz060/5336523 by The University of British Columbia Library user on 19 February 2019

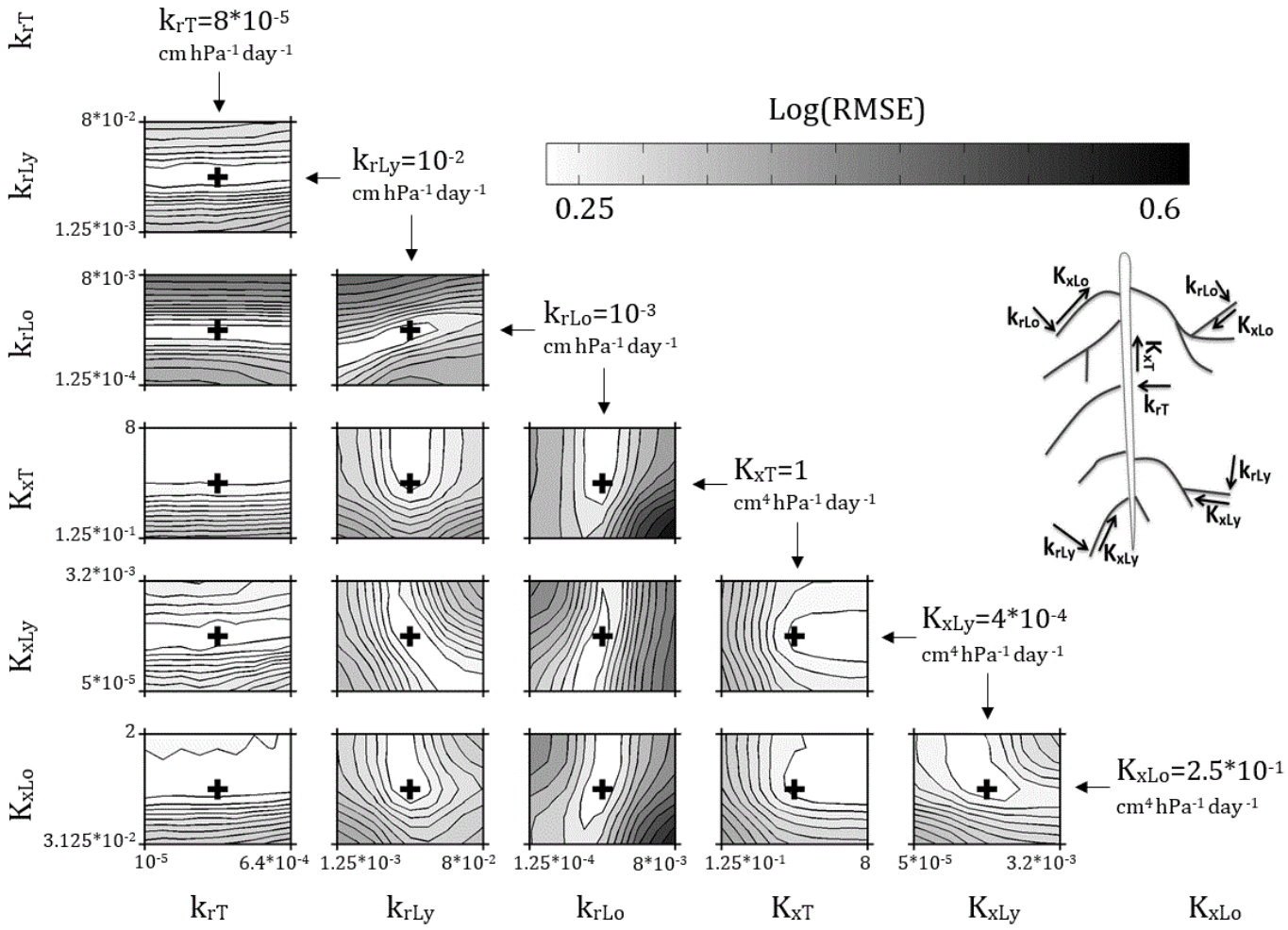

Figure 4

Black and white online and print

Accepted

Downloaded from https://academic.oup.com/jxb/advance-article-abstract/doi/10.1093/jxb/erz060/5336523 by The University of British Columbia Library user on 19 February 2019

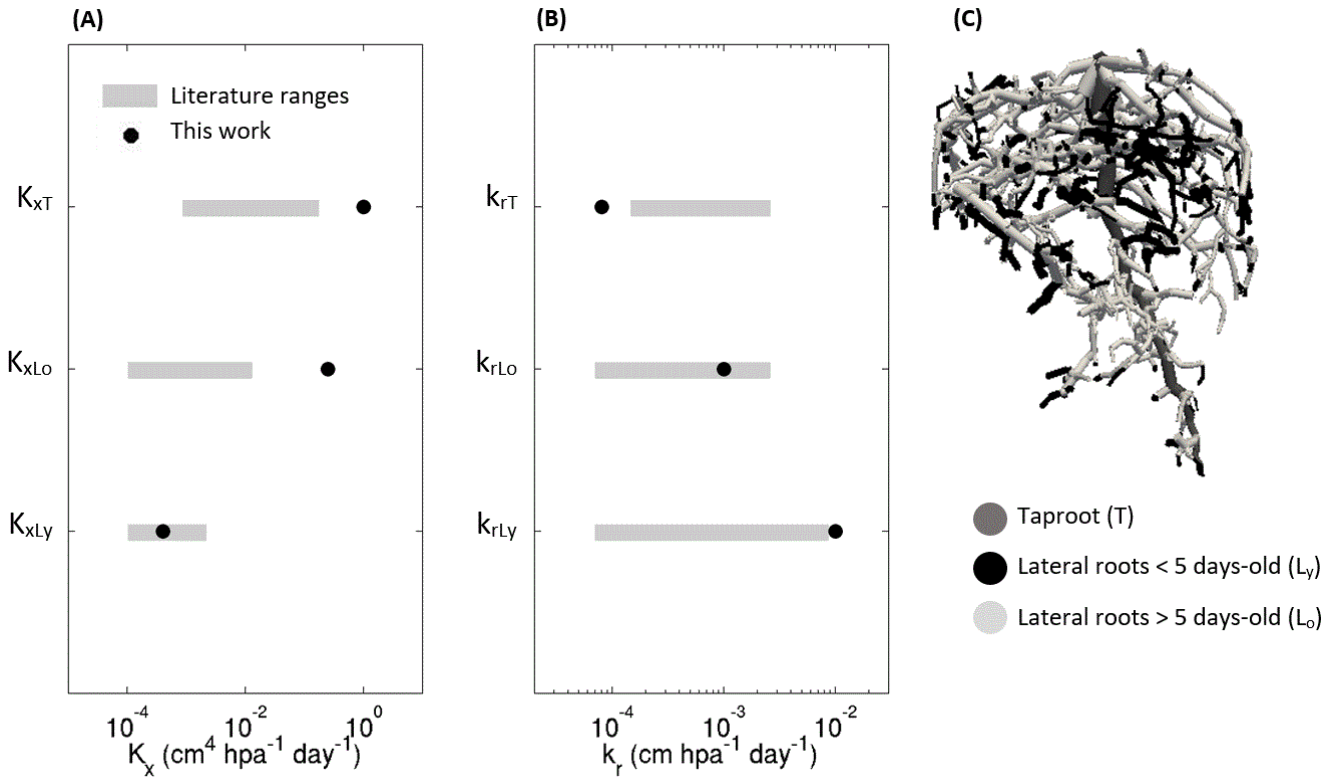

Figure 5

Black and white online and print

Accepted Ma

Downloaded from https://academic.oup.com/jxb/advance-article-abstract/doi/10.1093/jxb/erz060/5336523 by The University of British Columbia Library user on 19 February 2019

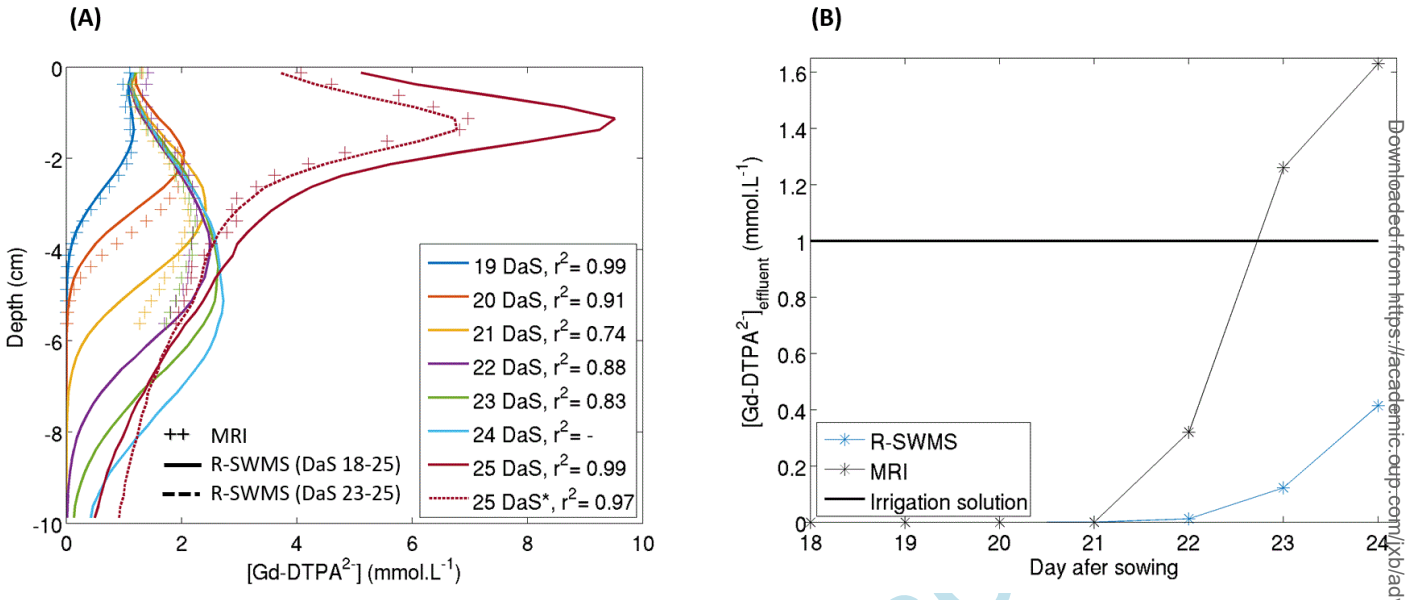

Figure 6

Color online, not print

Accepted Manuscript

Downloaded from https://academic.oup.com/jxb/advance-article-abstract/doi/10.1093/jxb/erz060/5336523 by The University of British Columbia Library user on 19 February 2019

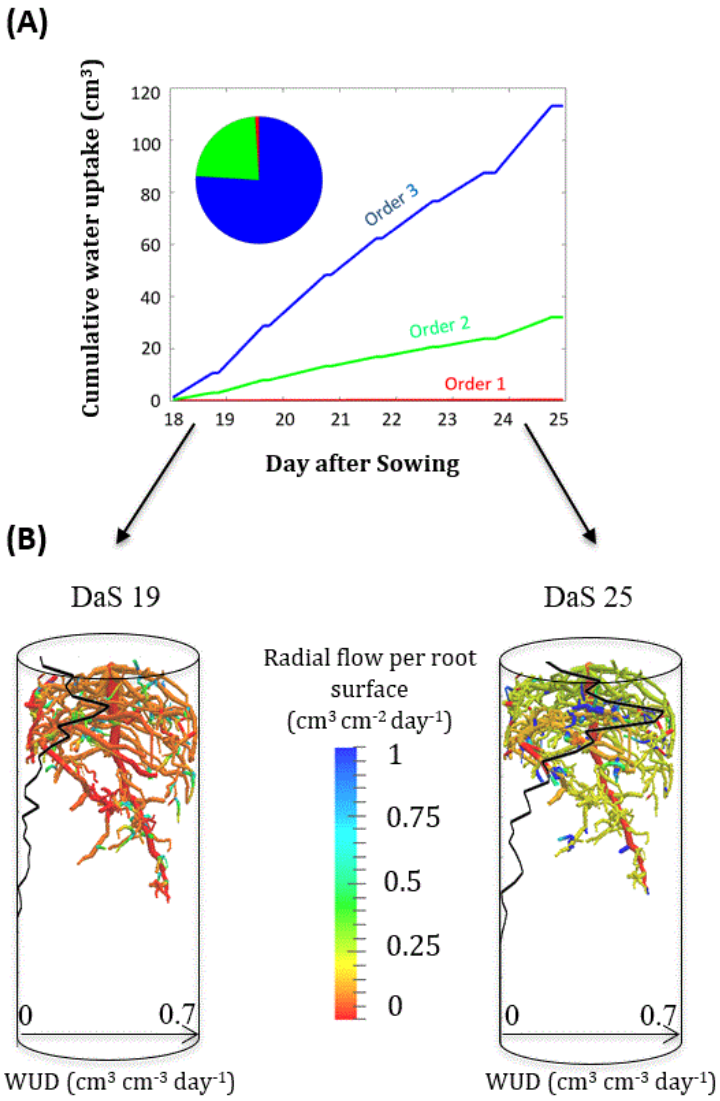

Figure 7

Color online, not print

Accepted Manuscript

Downloaded from https://academic.oup.com/jxb/advance-article-abstract/doi/10.1093/jxb/erz060/5336523 by The University of British Columbia Library user on 19 February 2019

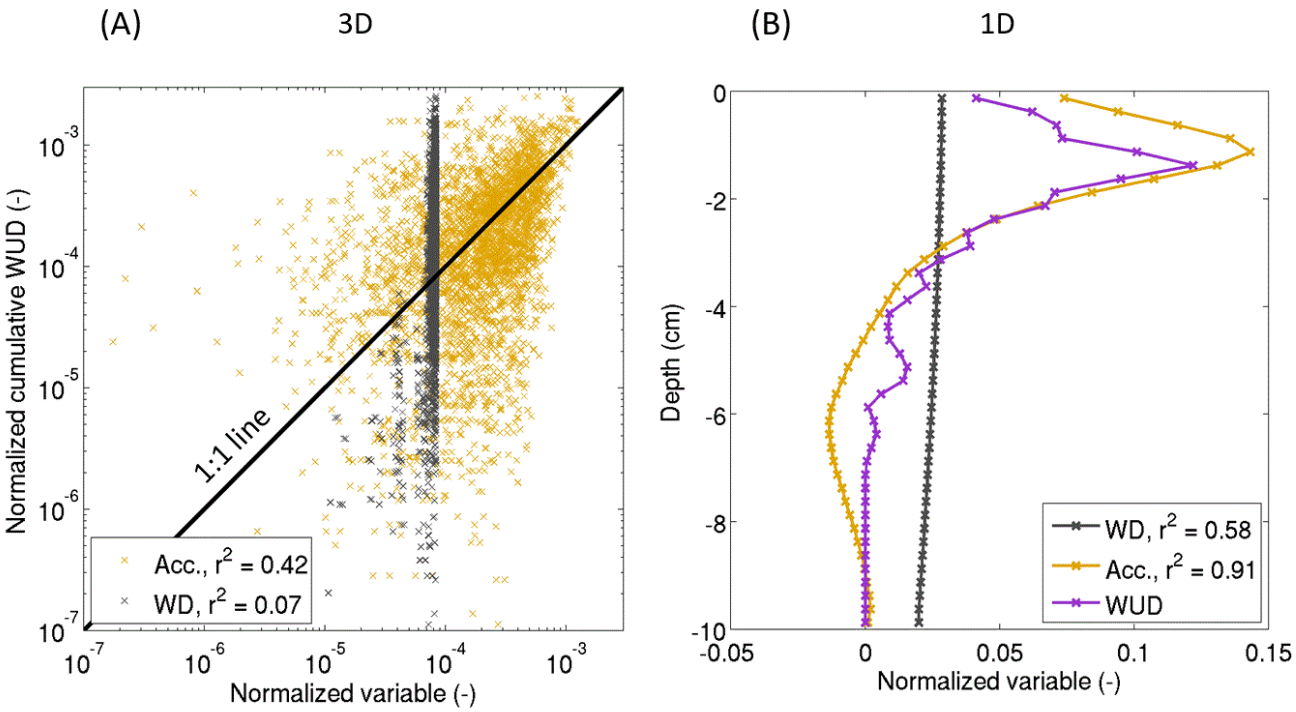

Figure 8

Color online, not print

Accepted Manuscript

Downloaded from https://academic.oup.com/jxb/advance-article-abstract/doi/10.1093/jxb/erz060/5336523 by The University of British Columbia Library user on 19 February 2019

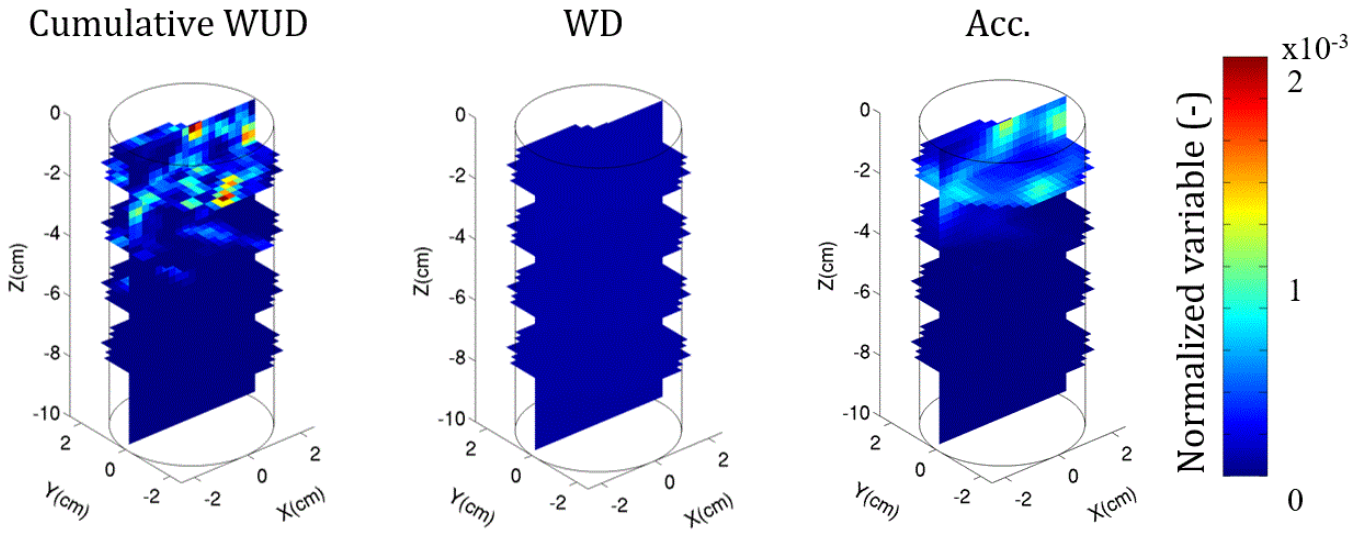

Figure 9

Color online, not print

Accepted Manuscript

Downloaded from https://academic.oup.com/jxb/advance-article-abstract/doi/10.1093/jxb/erz060/5336523 by The University of British Columbia Library user on 19 February 2019

Table 1. List of variables

Name	Symbol	Units	Description
Root axial conductance	K_x	$cm^4\ hPa^{-1}\ day^{-1}$	Root segment capacity to transport water axially
Root radial conductivity	k_r	$cm\ hPa^{-1}\ day^{-1}$	Root segment capacity to transport water radially
Root system total hydraulic conductance	K_{rs}	$m^3\ MPa^{-1}\ s^{-1}$	
Root system total hydraulic conductivity	k_{rs}	$m\ MPa^{-1}\ s^{-1}$	K_{rs} normalized by the total root surface
Water uptake density	WUD	$cm^3\ day^{-1}\ cm^{-3}$	The volumetric flow of uptake per soil voxel volume
Water depletion	WD	$cm^3\ cm^{-3}$	The water content change over successive observation times
Volumetric soil water content	θ	$cm^3\ cm^{-3}$	
Soil water potential	h	MPa	
Soil bulk density	ρ_b	$g\ cm^{-3}$	
Tracer concentration	[Gd-DTPA^{2-}]	$mmol\ L^{-1}$	
Tracer accumulation	Acc.	$mmol\ L^{-1}$	The increase of Gd-DTPA^{2-} concentration over the considered period
Solute longitudinal dispersivity	α_L	cm	
Solute lateral dispersivity	α_T	cm	

Accepted Manuscript

Downloaded from https://academic.oup.com/jxb/advance-article-abstract/doi/10.1093/jxb/erz060/5336523 by The University of British Columbia Library user on 19 February 2019